Optimization of a 6.78-MHz Inductive Power Transfer System for Unmanned Aerial Vehicles

Jiasheng Huang, *Graduate Student Member, IEEE*, Yi Dou, *Member, IEEE*, Xiaosheng Huang, *Member, IEEE*, Zhe Zhang, *Senior Member, IEEE*, Ziwei Ouyang, *Senior Member, IEEE*, and Michael A.E. Andersen, *Member, IEEE*

***Abstract*—This article presents an optimization of a 6.78-MHz inductive power transfer (IPT) system for unmanned aerial vehicles (UAVs). First, in order to mitigate the impact of the misalignment between the transmitting coil and the receiving coil on the output power and system efficiency, a homogeneous-flux transmitting coil was developed. The optimal allocation of turns of the transmitting coil for generating a homogeneous magnetic field was obtained using a built magnetic field and mutual inductance model combined with an optimization algorithm. In addition, an analytical eddy-current loss model of the air-core inductors was developed. Through the iterative processes for proximity-effect loss, the resistance modeling of the spiral and helical coils is improved, with errors of 7.1% and 4.9%, respectively. Then, the parameters of all the air-core inductors used in the study were optimized using the built loss model and optimization algorithm with various design considerations. Finally, a 6.78-MHz 200-W IPT system with a homogeneous-flux transmitting coil was demonstrated. The proposed system exhibited high-misalignment-tolerance and high-efficiency characteristics, maintaining an output power of approximate 200 W and an efficiency of 89% with a 25-mm lateral misalignment.**

***Index Terms*—Eddy-current loss, high misalignment tolerance, inductive power transfer (IPT), optimization, unmanned aerial vehicles (UAVs).**

I. Introduction

UNMANNED aerial vehicles (UAVs) have become increasingly popular in recent years due to their convenience in performing a variety of tasks, including power line inspection (see Fig. 1), monitoring, and so on [1], [2], [3], [4], [5], [6], [7], [8]. However, due to their small size and limited battery capacity, the operation time of photography UAVs is typically limited to approximate 30 min [9], [10], which is insufficient for heavy-load tasks, such as large-area or long-time inspections. To solve this problem, battery replacement is a straightforward method to prolong the operation time. However, this method requires human assistance. Alternatively, wired or wireless charging technology can be utilized to recharge the battery. By comparison, wireless charging technology is promising due to its convenience and safety characteristics [11].

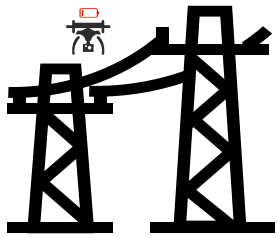

Fig. 1. Typical application scenarios of UAVs: power line inspection.

Wireless charging for UAVs can be achieved through two main methods: inductive power transfer (IPT) using a magnetic field [12], [13], [14], [15], [16], [17], [18], [19], and capacitive power transfer (CPT) utilizing an electrical field [20], [21], [22]. The use of wireless charging enables UAVs to operate without interruption of returning to the base for charging, which provides sufficient freedom [23]. However, one main challenge to implement IPT systems on UAVs is the misalignment between the transmitting coil on the charging platform and receiving coil on the UAVs, which results in a low efficiency and a unstable power transfer.

In recent years, there have been growing research interests in improving the misalignment tolerance of IPT systems for UAVs. Such efforts can be categorized into two main approaches as follows. 1) Utilize control strategies [2]. (2) Optimize the inductive coupler [13], [15], [16], [17], [18], [19]. In [2], based on the concept of nonlinear parity-time symmetry, a variable-frequency control approach was implemented to maintain a stable output and efficiency of the system despite different levels of lateral misalignment or transmission distance. However, the system complexity and cost were increased by the need for additional current sensing circuitries, including root mean square (rms) value calculation and zero-crossing detection, as well as a dead

Manuscript received 15 April 2023; revised 28 June 2023; accepted 16 July 2023. Date of publication 28 July 2023; date of current version 1 September 2023. Recommended for publication by Associate Editor Fei Lu. *(Corresponding authors: Yi Dou; Ziwei Ouyang.)*

Jiasheng Huang, Ziwei Ouyang, and Michael A.E. Andersen are with the Department of Electrical and Photonics Engineering, Technical University of Denmark, 2800 Kongens Lyngby, Denmark (e-mail: jiahuan@dtu.dk; ziou@dtu.dk; maea@dtu.dk).

Yi Dou is with the Resonant Link Inc., 8002 Zurich, Switzerland (e-mail: ydou@resonant-link.com).

Xiaosheng Huang is with the Fujian Provincial University Engineering Research Center for Industrial Automation, School of Electronic, Electrical Engineering and Physics, Fujian University of Technology, Fuzhou 350118, China (e-mail: hxs@fjut.edu.cn).

Zhe Zhang is with the State Key Laboratory of Reliability and Intelligence of Electrical Equipment, Hebei University of Technology, Tianjin 300130, China (e-mail: zhangzhedk@gmail.com).

Color versions of one or more figures in this article are available at https://doi.org/10.1109/TPEL.2023.3299833.

Digital Object Identifier 10.1109/TPEL.2023.3299833

time tuning circuit. Moreover, the output power of 10W was insufficient for fast charging of UAVs. In contrast, optimizing the magnetic coupler was shown to be a more cost-efficient solution. In [16], an 85-kHz, 200-W IPT system with an asymmetric magnetic coupler was constructed for drones. The transmitting coil formed by multiple groups of series circular coils was designed to generate a uniform horizontal magnetic field. However, the resulting misalignment tolerance ratio was only 11.1%. [17] proposed a novel squirrel-cage receiving coil to pick up multidimensional magnetic flux generated by the transmitting coil to improve the misalignment tolerance of the system. The misalignment tolerance ratio is up to 22.7%, but the peak efficiency is only 80%. In [18], a combined design of the transmitting coil, receiving coil, and onboard compensation coil was carried out to make the mutual inductance stable with different lateral misalignments. This approach resulted in a misalignment tolerance ratio of 50%, although with an efficiency of only 80.6%. The operation frequencies of the work in [16], [17], [18] fall within kHz range. In contrast, [13], [19] presented MHz-IPT systems for UAVs. Both 6.78 and 13.56 MHz frequencies belong to the industrial, scientific, and medical bands. Pushing frequencies to the MHz range allows for the elimination of magnetic cores and reduces the size of coils, which can be advantageous in decreasing the weight of the receiver on UAVs [24], [25]. The research work presented in [13] can achieve a high misalignment tolerance, but its implementation is limited due to a 13-W output power and 60% efficiency.

In this study, a homogeneous-flux transmitting coil is developed to keep the mutual inductance of the coupler stable with varying misalignment, thereby enhancing the misalignment tolerance of the system. Combining the built magnetic field and mutual inductance model and an optimization algorithm, such as Fmincon in MATLAB, the optimal allocation of turns for the transmitting coil was obtained. In addition, a loss model of the air-core inductor is built. Using the built loss model, the parameters of the air-core inductor have been comprehensively optimized to improve the quality factor and efficiency of the system. The main work and contributions of this study are given as follows.

1) Based on the model of the magnetic field and an optimization algorithm (Fmincon in MATLAB), a homogeneous-flux transmitting coil is designed. The validity of the proposed design is confirmed through finite element method (FEM) simulation and experimental measurement. Notably, the designed coil achieves a 25-mm lateral misalignment tolerance, corresponding to a 34.7% misalignment tolerance ratio.
2) A comprehensive analytical model for predicting eddy-current losses in air-core coil inductors has been developed. Through the utilization of iterative procedures for modeling the proximity-effect loss, the accuracy of the model has been improved and found to have an error of 7.1% for a planar spiral air-core inductor and 4.9% for a helical air-core inductor. Compared with using FEM simulations, employing the proposed analytical model can save a lot of computation time and resources while still providing accurate results.
3) By integrating the analytical loss model of the air-core inductor with an optimization algorithm, this study has optimized the parameters of all the utilized air-core inductors, leading to significant enhancements in both the quality factor and system efficiency. The outcome of this optimization effort is a demonstrated 6.78-MHz 200-W prototype that achieves a peak efficiency of 89%.
4) In summary, this research integrated various analytical models such as the magnetic field model and the proposed air-core inductor loss model to holistically optimize the parameters of the inductors and inductive coupler. The experimental results demonstrate the achievement of a high efficiency of 89% and a high misalignment tolerance ratio of 34.7% in an IPT system designed specifically for UAV applications.

The rest of this article is organized as follows. Section II outlines the circuit topology of the proposed IPT system, which comprises a push–pull class-E inverter, an LCC-S compensation network, an inductive coupler, and a passive push–pull class-E rectifier. Section III presents the design of the homogeneous-flux transmitting coil. Section IV describes the proposed analytical eddy-current loss model of the air-core inductor. An iterative process was employed to model the proximity-effect loss, thereby improving the accuracy of the model. In addition, this section provides the optimization and design flowcharts for all the utilized air-core inductors, which take into account different design considerations. In Section V, the built 200-W 6.78-MHz prototype of the IPT system is presented along with its test results. The proposed IPT system exhibits high-misalignment tolerance and high-efficiency characteristics. Finally, section VI concludes this article.

II. Circuit Topology of the IPT System

The circuit topology used in this study is illustrated in Fig. 2, which consists of a push–pull class-E inverter, an LCC-S compensation network, an inductive coupler, and a passive push–pull class-E rectifier.

A. Design of a Push–Pull Class-E Converter

The class-E inverter, illustrated in Fig. 3, is a promising topology for high-frequency IPT systems, in contrast to bridge-type inverters such as half-bridge and full-bridge inverters, as it only employs a single low-side switching device. However, the resonance results in the voltage of the switching devices exceeding the input dc voltage by several times. Consequently, to mitigate the stress on the devices, a push–pull topology comprising two class-E inverters with a 180° phase-shift, as depicted in Fig. 2, was implemented. In addition, interleaving two class-E converters in 180° phase-shift can suppress the odd-order harmonic through the dc source [26], [27]. Prior research in [27], [28], [29] indicates that satisfying the parameters of the components, as specified in (1), is essential for load-independent operation, constant voltage gain, and zero-voltage-switching (ZVS) across the entire load. In (1), V_{in} denotes the dc input voltage, P_{rated} represents the rated power of the converter, R_{rated} is the equivalent dc load resistance, ω_s is the operating angular

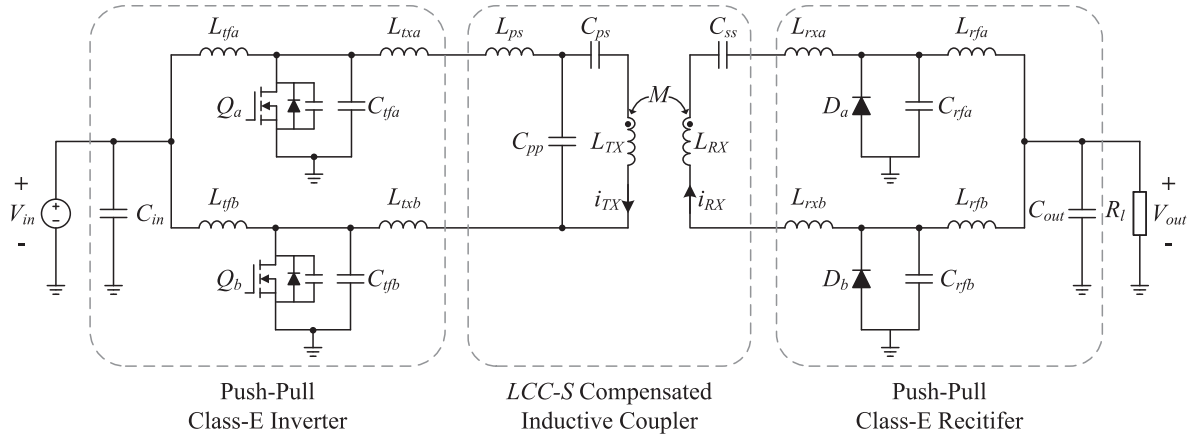

Fig. 2. Circuit topology of the proposed IPT system.

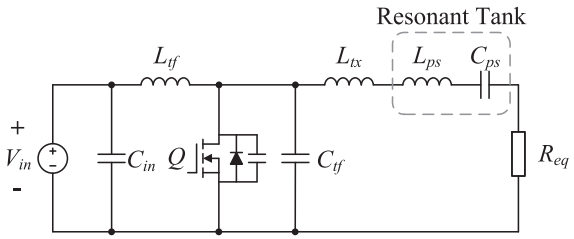

Fig. 3. Topology of the class-E inverter.

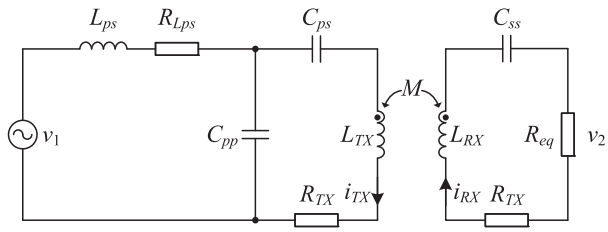

Fig. 4. Circuit of the LCC-S compensated inductive coupler.

frequency, $G_{\text{inv}} = 0.629125$ is the ratio of the dc input voltage to the amplitude of the ac voltage, and the $p_{\text{op}} = 1.647457$, $q = 1.291547$, $\xi = 0.266228$ are the optimal coefficients between the parameters. It is worth noting that the resonant capacitor $C_{tfa,b}$ also encompasses the output capacitance C_{oss} of the semiconductor devices

$$\begin{aligned} R_{\text{rated}} &= \frac{V_{\text{in}}^2}{0.5 \cdot P_{\text{rated}}} \\ L_{tfa,b} &= \frac{p_{\text{op}} \cdot R_{\text{rated}}}{2 \cdot \omega_s \cdot G_{\text{inv}}} \\ L_{txa,b} &= \xi \cdot L_{tf} \\ C_{tfa,b} &= \frac{1}{L_{tf} \cdot q^2 \cdot {\omega_s}^2} = \frac{G_{\text{inv}}}{R_{\text{rated}} \cdot p_{\text{op}} \cdot q^2 \cdot \omega_s}. \end{aligned} \tag{1}$$

To simplify the design of the push–pull class-E rectifier, it was decided to make its inductance equivalent to that of the push–pull class-E inverter. Nevertheless, the external parallel compensated capacitance is bound to differ, given that the equivalent capacitance of the switching devices differs from that of the SiC diodes. By employing circuit simulations based on the predetermined resonant parameters, output voltage, and power specifications, the voltage gain G_{rec} of the rectifier (the ratio of the dc output voltage to the amplitude of the ac voltage) can be obtained.

B. LCC-S Compensation

In this study, an LCC-S compensation topology, depicted in Fig. 4, has been utilized due to its load-independent voltage gain and zero-phase-angle (ZPA) features. The parameters of the compensation network should meet (2). Furthermore, the voltage gain of the compensation network can be evaluated via (3)

$$\omega_s = \frac{1}{\sqrt{L_{ps}C_{pp}}} = \frac{1}{\sqrt{(L_{TX} - L_{ps})C_{ps}}} = \frac{1}{\sqrt{L_{RX}C_{ss}}} \tag{2}$$

$$G_{\text{LCC}-S} = \frac{v_2}{v_1} = \frac{M}{L_{ps}} = \frac{k \cdot \sqrt{L_{TX}L_{RX}}}{L_{ps}}. \tag{3}$$

By integrating the abovementioned analysis, the overall voltage gain of the circuit can be calculated by

$$G_{\text{system}} = \frac{1}{G_{\text{inv}}} \cdot G_{\text{LCC}-S} \cdot G_{\text{rec}}. \tag{4}$$

Given that the LCC-S compensated inductive coupler serves as the intermediate stage of the system, the efficiency of this stage holds significant importance toward the overall system efficiency. The determination of the efficiency of the LCC-S compensated coupler can be calculated via [29]

$$\begin{aligned} \eta_1 &= \frac{Q_{RX}}{Q_{RX} + Q_L} \\ \eta_2 &= \frac{k^2}{k^2 + \frac{1}{Q_{TX}}(\frac{1}{Q_{RX}} + \frac{1}{Q_L})} \\ \eta_3 &= \frac{{k_{eq}}^2(\frac{1}{Q_{RX}} + \frac{1}{Q_L})}{{k_{eq}}^2(\frac{1}{Q_{RX}} + \frac{1}{Q_L}) + \frac{k^2}{Q_{Lps}} + \frac{Q_{RX}+Q_L}{Q_{Lps}Q_{TX}Q_{RX}Q_L}} \end{aligned}$$

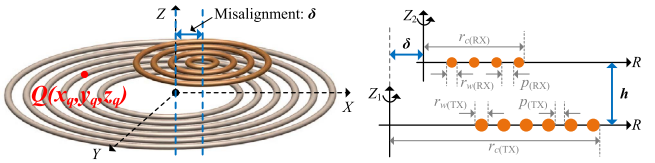

Fig. 5. Illustration of the inductive coupler. The misalignment, δ, is characterized as the lateral distance between the transmitting coil's and receiving coil's central axes. In addition, the transmission distance between the transmitting coil and receiving coil is denoted by the symbol h.

$$\eta_{\text{LCC}-S} = \eta_1 \cdot \eta_2 \cdot \eta_3 \tag{5}$$

where, $Q_{Lps} = \omega_s L_{ps}/R_{Lps}$, $Q_{TX} = \omega_s L_{TX}/R_{TX}$, $Q_{RX} = \omega_s L_{RX}/R_{RX}$, and $Q_L = \omega_s L_{RX}/R_{eq}$ are the quality factors of the compensation inductor L_{ps}, the transmitting coil L_{TX}, the receiving coil L_{RX}, and the loaded circuit, respectively; $k = \frac{M}{\sqrt{L_{TX}L_{RX}}}$ is the coupling coefficient of the inductive coupler; k_{eq} is the defined as $\sqrt{L_{ps}/L_{TX}}$.

III. Homogeneous-Flux Transmitting Coil Design

The misalignment between the transmitting coil and receiving coil has consistently posed a challenge in IPT systems, as it will reduce the coupling factor and affect the efficiency of the system. To address this issue and build a robust IPT system with high misalignment tolerance, a homogeneous-flux density transmitting coil was designed and implemented in this study.

A. Magnetic Field and Mutual Inductance Modeling

The inductive coupler is depicted in Fig. 5, showing both its 3-D and 2-D cross-sectional views. The misalignment, δ, is characterized as the lateral distance between the transmitting coil's and receiving coil's central axes. In addition, the transmission distance between the transmitting coil and receiving coil is denoted by the symbol h. Based on the Biot–Savart law, the magnetic field generated by the transmitting coil at the point $Q(x_q, y_q, z_q)$, $\vec{B}(x_q, y_q, z_q)$ and its vertical component (parallel to the Z-axis), $\vec{B_z}(x_q, y_q, z_q)$, can be calculated by

$$\vec{B}(x_q, y_q, z_q) = \sum_{i=1}^{n_{TX}} \frac{\mu_0}{4\pi} \int_0^{2\pi} \frac{\vec{I}(\theta) \times \vec{R}(x_q, y_q, z_q, r_i, \theta)}{R^3(x_q, y_q, z_q, r_i, \theta)} \mathrm{d}\theta$$

$$\vec{I}(\theta) = \begin{bmatrix} -\sin(\theta) \\ \cos(\theta) \\ 0 \end{bmatrix}, \quad \vec{R} = \begin{bmatrix} x_q - r_i \cdot \cos(\theta) \\ y_q - r_i \cdot \sin(\theta) \\ z_q \end{bmatrix}$$

$$\vec{B_z}(x_q, y_q, z_q) = \vec{B}(x_q, y_q, z_q) \cdot \left[0, 0, 1\right]^{\mathrm{T}} \tag{6}$$

given that I represents the unit current flowing through the coil and r_i denotes the radius of each turn. Then, the mutual inductance of the inductive coupler can be derived as

$$M = \frac{\Phi}{I} = \frac{\sum_{k=1}^{n_{RX}} \iint_{S_{RX}(k)} \vec{B_z}(x, y, h) \mathrm{d}S}{I} \tag{7}$$

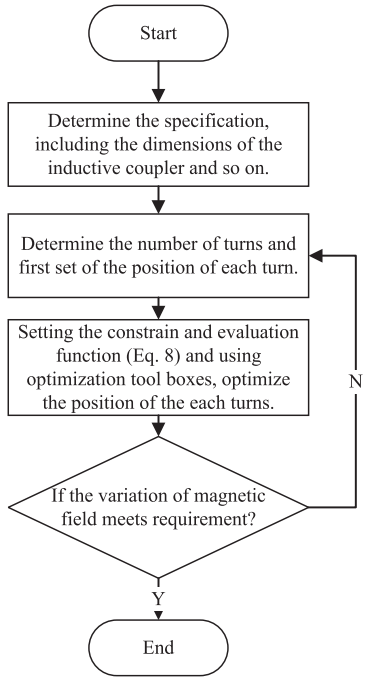

Fig. 6. Design flowchart of the homogeneous-flux transmitting coil.

where, $\vec{B_z}(x, y, h)$ is the magnetic field component parallel to the Z-axis at the plane $\mathrm{Z} = h$, and $S_{RX}(k)$ represents the coverage region of each turn of the receiving coil. It can be found that the constancy of the mutual inductance between the transmitting and receiving coils is contingent upon a constant magnetic field generated by the transmitting coil when the receiving is fixed. Therefore, a homogeneous-flux transmitting coil is developed in this study.

B. Placement of the Turns of the Transmitting Coil

In this study, a homogeneous magnetic field by the transmitting coil within a predefined region can be achieved by strategically placing each turn of the transmitting coil at the required position. To derive a magnetic field generated by a coil, there are usually two methods can be used, i.e., FEM simulations and an analytical model based on the Biot–Savart law. Using FEM simulations is a more general approach, particularly for irregular simulation models, but it is often time-consuming. In addition, combining FEM simulations and an optimization algorithm for optimizing the placement of each turn of the transmitting coil will be complex. Thus, this study employs a Biot–Savart law-based analytical model combined with an optimization algorithm. The design flowchart of the transmitting coil for generating a homogeneous magnetic field is illustrated in Fig. 6, which comprises the following steps.

1) *Step 1:* In accordance with the given application, the initial step involves the determination of the size of the transmitting coil, the appropriate distance between the transmitting and receiving coils, the necessary misalignment tolerance, as well as the target variation of the magnetic field at the specified region.

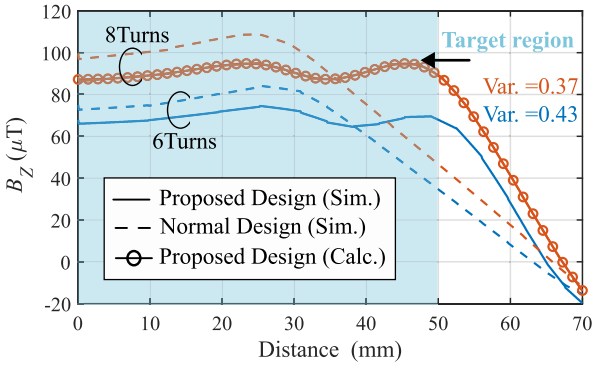

Fig. 7. Simulation and calculation of the magnetic field at the plane which is 10 mm away from the plane of the transmitting coil. The excitation current is 1 A. Since the generated magnetic field is symmetry, the plot of the field can be simplified into 2-D view. The x-axis of the figure means horizontal misalignment refer to the center of the transmitting coil. The orange lines represent the transmitting coil with eight turns and blue lines represent the transmitting coil with six turns. The eight-turn normal design of the transmitting coil with the turns' radii array of [30.4, 36.34, 42.28, 48.23, 54.17, 60.11, 66.06, 72.0] (mm). The eight-turn proposed homogeneous-flux transmitting coil with the turns' radii array of [30.4, 51.0, 54.5, 58.0, 61.5, 65.0, 68.5, 72.0] (mm).

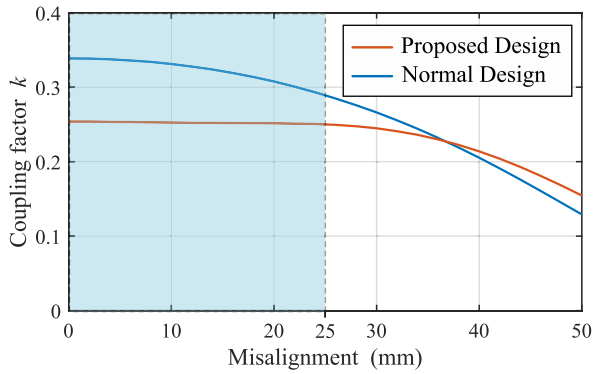

Fig. 8. Coupling factors by FEM simulations versus misalignments. The distance between the transmitting coil and receiving coil is 10mm. The turns' radii array of the receiving coil is [20.0, 22.0, 24.0, 26.0, 28.0, 30.0, 32.0, 34.0] (mm). The blue line represents normal design of the transmitting coil with the turns' radii array of [30.4, 36.34, 42.28, 48.23, 54.17, 60.11, 66.06, 72.0] (mm). The orange line represents proposed homogeneous-flux transmitting coil with the turns' radii array of [30.4, 51.0, 54.5, 58.0, 61.5, 65.0, 68.5, 72.0] (mm).

2) *Step 2:* Determine the number of turns, and give the initial set of the position of each turn.
3) *Step 3:* Set the constrain function, e.g., the minimal distance between each of two adjacent turns; Use the optimization algorithm, e.g., Fmincon in MATLAB, to obtain the optimal allocation of turns, which gives the minimal variation of the magnetic field density at the required region, as shown in

$$\min \ f(x) = \frac{\sigma(B_z(x,q))}{\overline{B}_z(x,q)}, q \in [0,d]$$
$$\text{s.t.} \quad 0 < x_i < x_{i+1} \tag{8}$$

where, $\sigma(B_z)$ and $\overline{B}_z$ represent the standard deviation and mean of the generated magnetic field, respectively. (The variation of the magnetic field is evaluated by the standard deviation divide by the average value.)
4) *Step 4:* If the magnetic field variation generated by the current design falls below the predetermined requirement, the design process is deemed finalized. Conversely, if the variation fails to meet the target, the iterative design process must recommence at step 2, with adjustments made to the number of turns.

C. Verification

Fig. 7 illustrates the magnetic field generated by four different transmitting coils. The dashed lines correspond to coils with a normal distribution of turns, while the solid lines correspond to coils with optimal allocation obtained by the optimization algorithm. Notably, the analytical-based calculation results align closely with the FEM simulation results (ANSYS MAXWELL is used in this study), signifying the potential of replacing FEM simulations with the analytical model for optimization purposes. Moreover, compared the magnetic field of the design with a traditional uniform allocation of the winding, the field by the coil with the optimal allocation of the winding remains relatively flat, resulting in a more stable mutual inductance of the coupler when facing misalignment between the transmitting coil and receiving coil. What is more, increasing the number of turns from 6 to 8 could improve the amplitude of the magnetic field, and reduce the variation as well.

Fig. 8 presents the FEM simulation results of the coupling factor of the inductive coupler with different misalignments. It can be seen that, compared with the normal design (even distribution of the turns), the proposed homogeneous-flux transmitting coil could improve the misalignment tolerance of the coupler, i.e. the coupling factor could be kept nearly constant when the misalignment is below 25 mm.

IV. Optimization of the Air-Core Inductor

In the last section, the optimization of the transmitting coil was carried out to enhance the misalignment tolerance of the IPT system. Besides misalignment tolerance, the efficiency of the system is also a critical performance indicator. This section begins with developing a loss model for spiral and helical air-core inductors. Subsequently, an analytical model-based optimization is employed to improve the quality factor of the air-core inductors, thereby improving the efficiency of the system.

A. Eddy-Current Losses in Round Conductors

The conduction loss of an air-core inductor comprises two parts: skin-effect loss and proximity-effect loss, which are validated to be decoupled by each other [30]. In this article, we will separately model these two effects and combine the results to derive the total loss. It needs to be noted that the built model is based on infinite long conductors with round cross sections, as shown in Fig. 9. Then according to the dimension of the coil, derive its corresponding resistance.

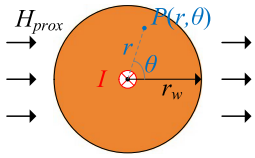

Fig. 9. 2-D illustration for infinitely long conductor with round cross-section. The radius of the conductor is r_w. The current through the conductor is unit current I (magnitude $\hat{I}$). To simplify the model, the H_{prox} (magnitude $\hat{H}_{\text{prox}}$) is assumed as constant.

Fig. 10. Illustration for two types of air-core inductors used in this study. (a) Structure of a helical coil and its simplified 2-D cross-section view. (b) Structure of a spiral coil and its simplified 2-D cross-section view.

Considering the eddy-current effect, the current density J at the point $P(r,\theta)$ can be calculated as [30], [31]

$$J_{\text{skin}}(r,\theta) = \frac{\hat{I} i^{\frac{3}{2}} k}{2\sqrt{2}\pi r_w} \frac{\mathbb{J}_0(i^{\frac{3}{2}} k r)}{\mathbb{J}_1(i^{\frac{3}{2}} k r_w)}$$

$$J_{\text{prox}}(r,\theta,H_{\text{prox}}) = \frac{2\mu_0{}^2 i^{\frac{3}{2}} k r_w \hat{H}_{\text{prox}} \mathbb{J}_1(i^{\frac{3}{2}} k r_w r)}{\mathbb{J}_0(i^{\frac{3}{2}} k r_w{}^2)} \sin(\theta)$$

$$k = \sqrt{w_s \mu_0 / \rho} \tag{9}$$

where, $\mathbb{J}_0$ and $\mathbb{J}_1$ are the 0th and 1st order of Bessel functions of the first kind, ρ is the resistivity of the conductor material, μ_0 is the vacuum magnetic permeability. Then the resulting eddy-current loss per unit length can be calculated as

$$P_{\text{eddy-loss}} = \frac{\rho}{2} \int_0^{2\pi} \int_0^{r_w} |J|^2 r \mathrm{d}r \mathrm{d}\theta \tag{10}$$

where, the J can be replaced by J_{skin} for skin-effect loss and J_{prox} for proximity-effect loss, respectively. After mathematical conversions, the skin-effect and proximity-effect loss can be rewritten as

$$P_{0(\text{skin})} = \frac{\rho}{\pi r_w{}^2} \cdot \frac{\xi}{4\sqrt{2}} \left(\frac{\text{ber}_0(\xi)\text{bei}_1(\xi) - \text{ber}_0(\xi)\text{ber}_1(\xi)}{\text{ber}_1(\xi)^2 + \text{bei}_1(\xi)^2} - \frac{\text{bei}_0(\xi)\text{ber}_1(\xi) + \text{bei}_0(\xi)\text{bei}_1(\xi)}{\text{ber}_1(\xi)^2 + \text{bei}_1(\xi)^2} \right) \cdot \hat{I}^2$$

$$P_{0(\text{prox})} = -\sqrt{2}\pi\xi\rho \left(\frac{\text{ber}_2(\xi)\text{ber}_1(\xi) + \text{ber}_2(\xi)\text{bei}_1(\xi)}{\text{ber}_0(\xi)^2 + \text{bei}_0(\xi)^2} - \frac{\text{bei}_2(\xi)\text{bei}_1(\xi) - \text{bei}_2(\xi)\text{ber}_1(\xi)}{\text{ber}_0(\xi)^2 + \text{bei}_0(\xi)^2} \right) \cdot \hat{H}_{\text{prox}}^2. \tag{11}$$

B. Loss Modeling on Air-Core Inductors

Fig. 10 depicted two types of air-core inductors used in this study, the helical coil and planar spiral coil, respectively. Based on the eddy-current loss model of the round conductors, the total power loss on the air-core inductor can be derived as

$$P_{\text{loss(Helical)}} = \sum_{i=1}^{n} (P_{0(\text{skin})} + P_{0(\text{prox})}) \cdot (2\pi r_c)$$

$$P_{\text{loss(Spiral)}} = \sum_{i=1}^{n} (P_{0(\text{skin})} + P_{0(\text{prox})}) \cdot (2\pi r_i). \tag{12}$$

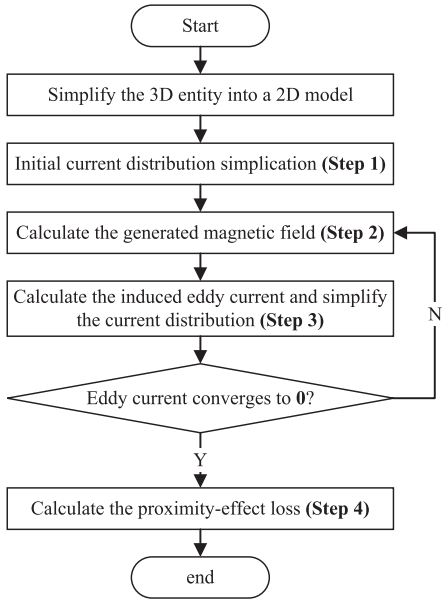

Fig. 11. Illustration for the iterative process for the proximity-effect loss calculation.

The skin-effect loss can be calculated based on the geometry of the coil by the initial model in (11). Nevertheless, the effort is still needed to deal with the proximity-effect loss since it is related to the external magnetic field H_{prox}. To this end, this study proposes an iterative calculation method for modeling the proximity-effect loss of an air-core inductor, as illustrated in Fig. 11. In addition, it is worth noting that the proposed modeling concept can be applied to other air-core inductors/coils, provided that the windings are composed of round solid wire. To expound on the iterative proximity-effect loss calculation process, we employ a four-turn helical coil as an example and present the details of each step in Fig. 12, which are described as follows.

1) *Step 1:* The illustration displays four turns that are arranged in a line parallel to the *Z*-axis. These turns have identical coil radius r_c and wire radius r_w. In order to apply the Biot–Savart law, the current through each turn is considered to be a filament current concentrated at the center of the round cross-section. The illustration denotes the currents as $I_{0,\text{N1}}$–$I_{0,\text{N4}}$, signifying the initial currents for the 0th iteration on the turns labeled as N1–N4.
2) *Step 2:* The estimation of H_{prox} is necessary for the calculation of proximity-effect eddy current and loss, as given in (9) and (11). The assumption is made that the H_{prox} equals to the field generated at the center of each cross-section

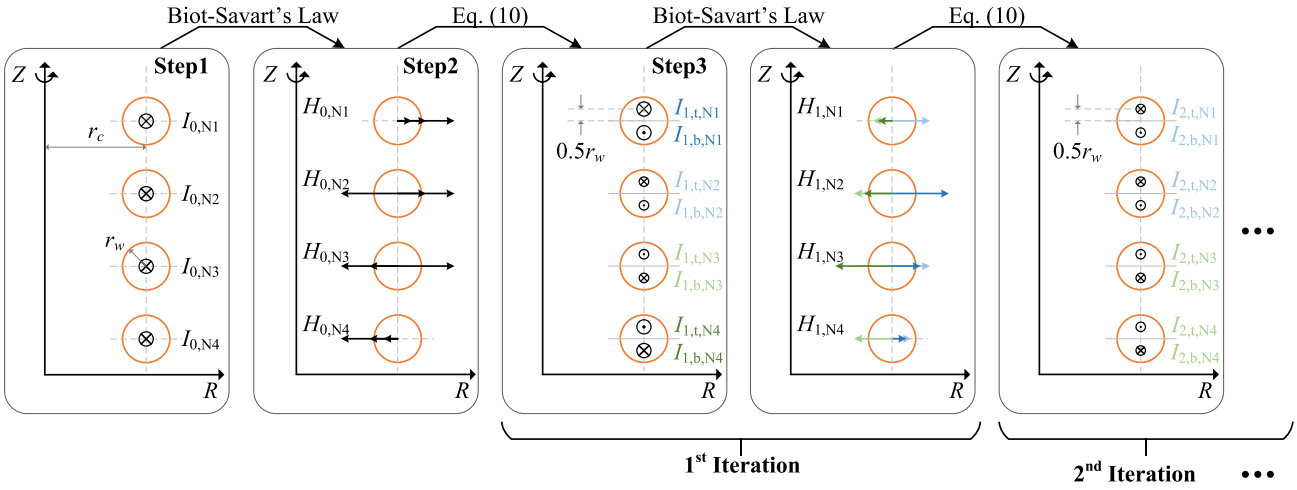

Fig. 12. Illustration for the detail of the iterative process for the proximity-effect loss calculation.

of the turns by all the filament currents from step 1. The H_{prox} can be calculated by applying the Biot–Savart law. For instance, the H_{prox} cutting the turn N1 ($H_{0,\text{N1}}$) equals to the total flux generated by the current $I_{0,\text{N2}}$, $I_{0,\text{N3}}$, and $I_{0,\text{N4}}$. Once the H_{prox} cutting the winding is obtained, the induced proximity-effect eddy-current can be calculated based on the model in (9), and the corresponding loss can be obtained by (11) as well.

3) *Step 3:* The H-field generated by the induced eddy-current, which cuts the winding reversely, was not considered in step 2. In this step, the induced eddy-current was simplified into two filamentary currents, such as $I_{1,\text{t,N1}}$ and $I_{1,\text{b,N1}}$ at the turn N1, for the 1st iteration. The amplitudes of these two filamentary currents are equal to the integral of the current density at the top half-cross-section and the bottom half-cross-section. Moreover, the position chosen for the filamentary current is $\pm 0.5 r_w$ away from the center of the cross-section. Then, go back to step 2 to calculate the generated magnetic field and proximity-effect loss correspondingly. The process of step 2 and step 3 should be applied iteratively until the induced eddy current converges to zero.
4) *Step 4:* Summarize all the iterative results to get the total proximity-effect loss.

C. Modeling Verification

In order to assess the applicability of the proposed model for calculating resistance in the helical and spiral air-core inductors utilized in this study, a comparison is made between the modeled results and those obtained via FEM simulations. A fine mesh is employed over the conductor in the FEM simulations to ensure precise simulation outcomes. The cross-section view of the mesh allocation and current density simulation result is given in Fig. 13. Fig. 14 presents the comparison results, indicating a high level of agreement between the proposed model and the simulation.

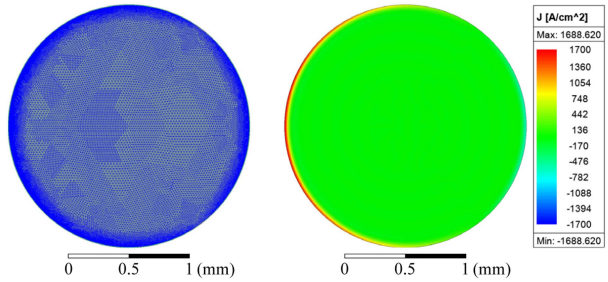

Fig. 13. Illustration for mesh allocation and current density result in the FEM simulation. The left figure shows the mesh allocation. The right-hand side figure shows the current density over the conductor.

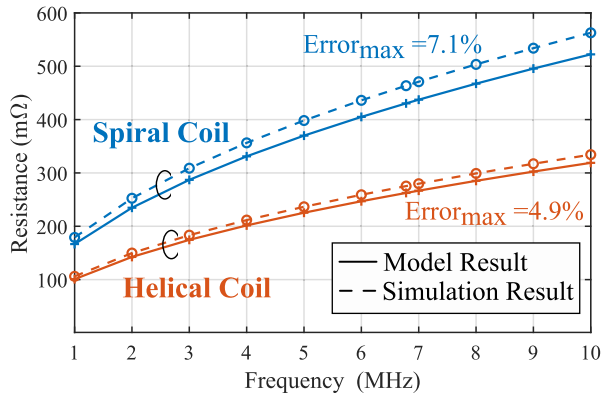

Fig. 14. Comparison between FEM simulations and model results. (The parameters of the spiral air-core inductor: $r = [43.5, 48, 52.5, 57, 61.5, 66, 70.5, 75]$(mm), $r_w = 1$(mm). The parameters of the helical air-core inductor: $r_c = 20$ mm, $r_w = 0.5$ mm, $p_c = 2$ mm. The convergence of error in FEM simulations is 0.002%.).

D. Air-Core Inductor Design Consideration

Based on the analytical model, including the resistance, and inductance of the air-core inductor, the parameters of the coil can be optimized with different design considerations. The optimization of the air-core inductors in this study is depicted in Fig. 15, and an example of optimizing the parameters of the air-core inductor in the push–pull class-E converter is presented

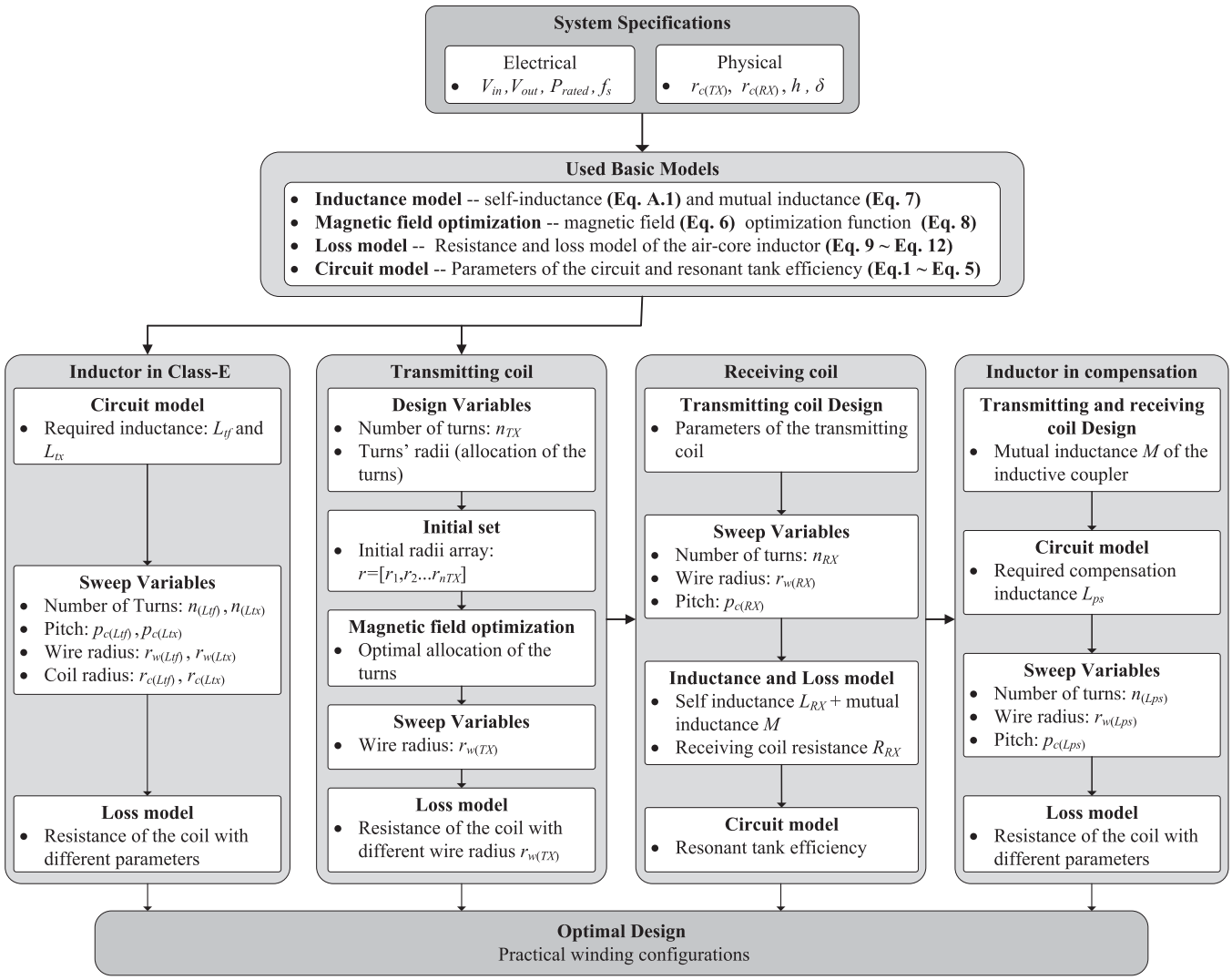

Fig. 15. Optimization of the air-core inductors in the proposed system.

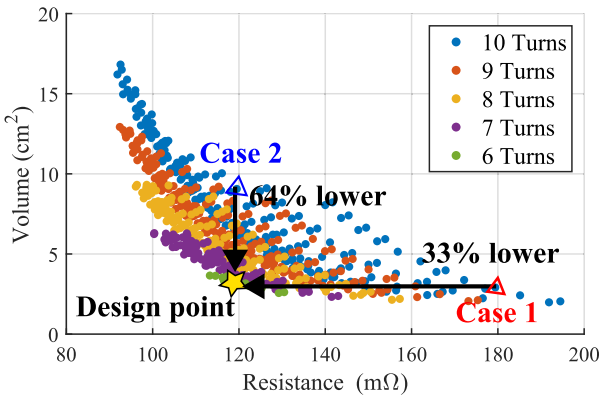

Fig. 16. Example of optimizing the air-core inductor in the class-E converter.

in Fig. 16. The description of the air-core inductor optimization is presented as follows.

1) *Air-core inductors in the class-E converter:* For an air-core inductor, a larger component volume typically results in a higher quality factor. However, it is insufficient to solely consider the quality factor without taking into account the power density of the converter. Therefore, the optimal design of an inductor in a class-E converter should balance the quality factor and volume while meeting the required inductance value for circuit operation. This multiobjective problem can be solved based on the analytical models of the inductance and resistance combined with an optimization toolbox. The optimization results are shown in Fig. 16, where all points meet the inductance requirement for the class-E converter design. However, different sets of parameters lead to varying coil resistance and volume. Considering the power density and efficiency, the design point can be selected. Comparing the optimal design with one of the 10-turn solutions (Case 1 denoted by a red triangle), it is evident that they have similar volumes, but the optimal design exhibits 33% lower resistance, leading to improved efficiency. When compared to another design with the same resistance (Case 2 denoted by a blue triangle), the optimal design has a significantly smaller

TABLE I
OPTIMIZATION RESULTS OF THE AIR-CORE INDUCTORS

Description	Symbols	Inductance*	Q*	f_r*	Structure parameters
Inductors in Class-E converters	$L_{tf(a,b)}/L_{rf(a,b)}$	664.6 nH	220	>110 MHz	Helical air-core inductor, six turns, $r_w = 10.3$mm, $r_c = 0.55$mm, $p_c = 2.0$mm
	$L_{tx(a,b)}/L_{rx(a,b)}$	184.2 nH	130	>110 MHz	Helical air-core inductor, four turns, $r_w = 6.50$mm, $r_c = 0.40$mm, $p_c = 2.3$mm
Inductor in comp.	L_{ps}	1.6 µH	284	>110 MHz	Helical air-core inductor, eight turns, $r_w = 15.0$mm, $r_c = 0.55$mm, $p_c = 3.0$mm
Transmitting coil	L_{TX}	10.4 µH	333	25.6 MHz	Spiral air-core inductor, $r_w = 1$mm Turns' radii = [30.4, 51.0, 54.5, 58.0, 61.5, 65.0, 68.5, 72.0] mm
Receiving coil	L_{RX}	4.4 µH	266	55.3 MHz	Spiral air-core inductor, $r_w = 0.55$mm Turns' radii = [20.0, 22.0, 24.0, 26.0, 28.0, 30.0, 32.0, 34.0] mm

* The data are measured by impedance analyzer Agilent 4294A at 6.78MHz.

TABLE II
SPECIFICATIONS OF THE IPT PROTOTYPE

Parameters	Values	Description
V_{in}	48V	Input voltage
f_s	6.78MHz	Operating frequency
V_{out}	48V	Rated output voltage
P_{rated}	200W	Rated output power
$Q_{a(b)}$	GS66508T	Switching devices in the inverter
	LMG1210	Gate driver in the inverter
$D_{a(b)}$	C3D10060A	Diodes in the rectifier
$C_{tf(a,b)}$*	512pF	Capacitor in the Class-E converter
C_{pp}**	330.4pF	Capacitor in the primary compensation
C_{ps}**	57pF	Capacitor in the primary compensation
C_{ss}**	119.2pF	Capacitor in the secondary compensation

* The capacitance includes the parasitic capacitor of the semiconductor and external ceramic capacitor.
** The capacitor are from ATC 800R series.

volume, reduced by 64%, thereby enhancing the power density of the system.

2) *Transmitting coil:* The parameters of the transmitting coil are mostly established in Section III, with the exception of the wire radius of the conductor. As such, the transmitting coil design procedure prioritizes compliance with the misalignment tolerance specifications before optimizing the wire radius for improving the quality factor.
3) *Receiving coil:* As indicated in (5), the efficiency of the resonant tank is affected by both the inductance and quality factor of the receiving coil. Therefore, the optimization of the receiving coil aims to enhance the efficiency of the resonant tank. Initially, the parameters of the receiving coil are swept, and the inductance and quality factor of the coil are derived using the inductance model and the analytical loss model. Subsequently, the circuit model in (5) is employed to determine the efficiency of the resonant tank and the optimal set of parameters leading to the highest efficiency is selected.
4) *Inductor of the LCC-S compensation network:* With the specific design of the transmitting coil and receiving coil, the mutual inductance of the inductive coupler can be derived according to (6) and (7). To achieve a predetermined voltage gain, the required compensation inductance can be calculated using (3). Consequently, optimizing the inductor in the LCC-S compensation network involves considering the inductance requirement for the voltage gain, as well as the structural parameters, such as the number of turns, coil radius, wire radius, and pitch, for improving the quality factor.

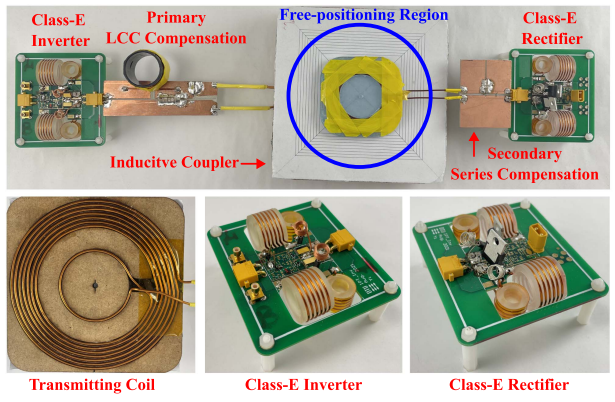

(a)

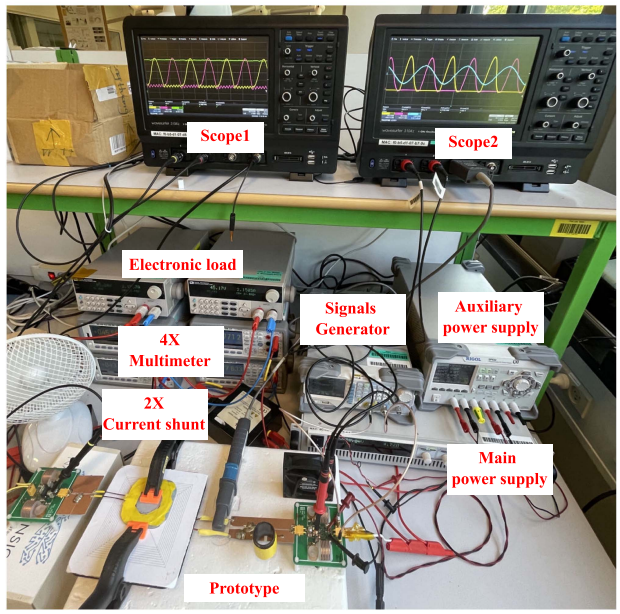

(b)

Fig. 17. Prototype and measurement setup. (a) Prototype of the proposed IPT system. (b) Measurement setup when system is running.

Following optimization, the parameters of the air-core inductors used in this study, and their corresponding measurement results, are listed in Table I.

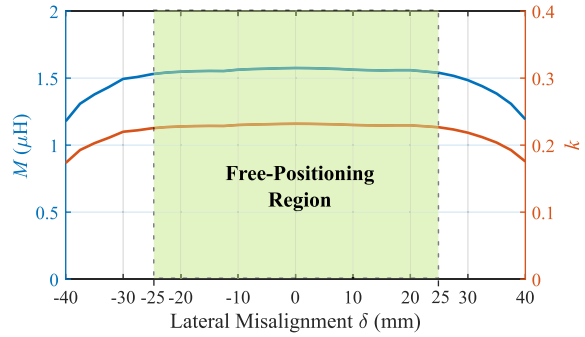

Fig. 18. Inductive coupler measurement result with different misalignment. The distance between the transmitting coil and receiving coil is fixed as 1 cm. The blue solid line represents the mutual inductance of the coupler versus different misalignment. The orange solid line represents the coupling coefficient versus different misalignment.

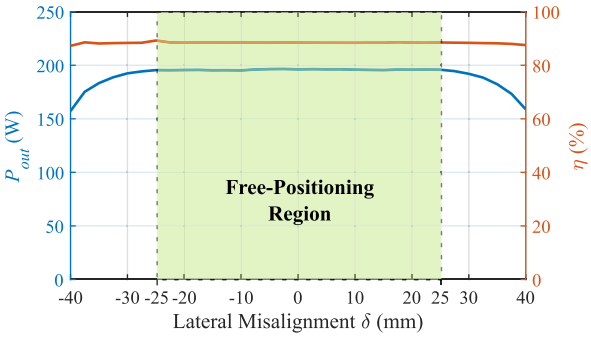

Fig. 19. Circuit test results, when keeping input voltage as $V_{\text{in}} = 48$ V and resistive load as $R_l = 10.5\,\Omega$. The blue solid line represents output power versus misalignment. And the orange solid line represents system efficiency versus misalignment.

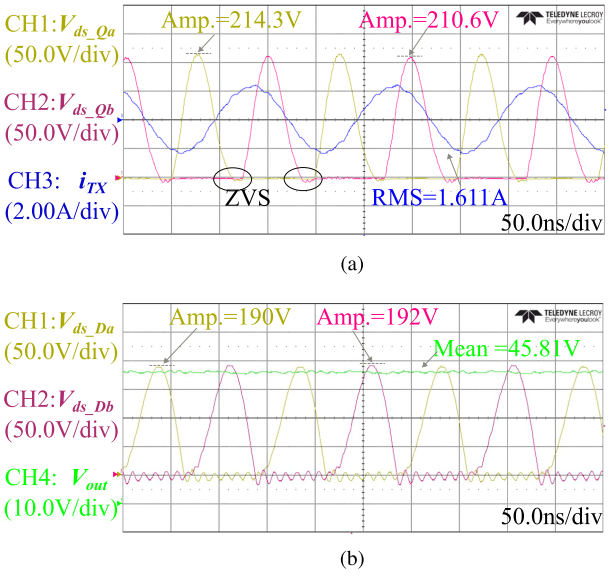

Fig. 20. Experimental waveforms when the inductive coupler is aligned. (a) Measured drain-source voltage of the inverter and current through the transmitting coil. (b) Measured diode voltage of the rectifier and output voltage.

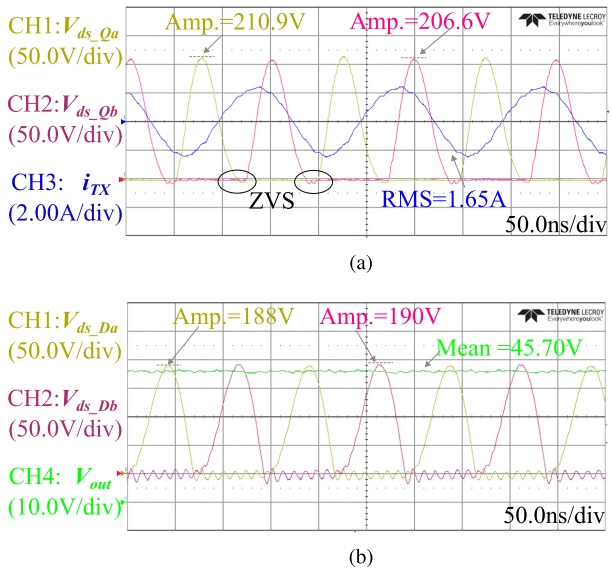

Fig. 21. Experimental waveforms with 25-mm lateral misalignment. (a) Measured drain-source voltage waveform of the inverter and current through the transmitting coil. (b) Measured diode voltage of the rectifier and output voltage.

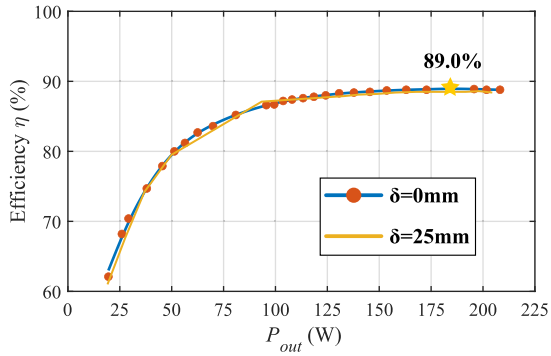

Fig. 22. Efficiency curves when the inductive coupler is aligned and 25-mm lateral misaligned.

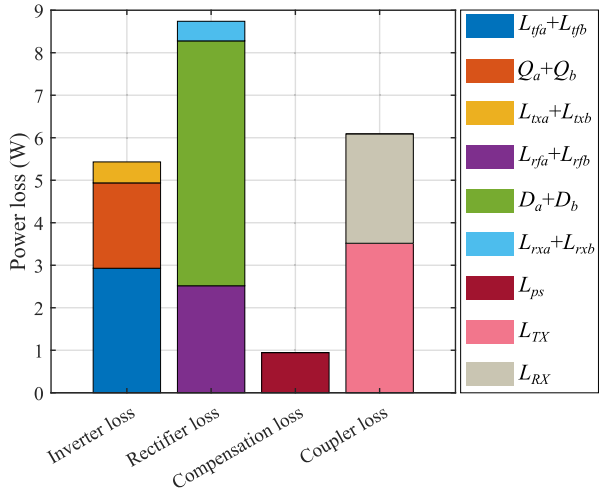

Fig. 23. Power losses breakdown of the prototype at rated power output.

TABLE III
COMPARED WITH THE REPORTED IPT SYSTEMS FOR UAVS

Reference	Operating frequency	Power	Efficiency	Transmitting coil radius	Receiving size	Lateral misalignment tolerance δ	Misalignment tolerance ratio*
[15]	85kHz	200W	90%	180mm	20mm × 40mm	±20mm	11.1%
[16]	500kHz	128.2W	89%	500mm	50mm × 200mm	±20mm	8%
[17]	85kHz	135.8W	80%	220mm	20mm × 200mm	±50mm	22.7%
[18]	150kHz	150W	80.6%	280mm	Radius 80mm	150mm	50%
[13]	13.56MHz	13W	≈ 60%	100mm	110mm × 110mm	±75mm	75%
This work	6.78MHz	200W	89.0%	72mm	Radius: 34mm	25mm	34.7%

* The misalignment tolerance ratio is defined as the lateral misalignment tolerance divided by the dimension of the transmitting coil.

V. EXPERIMENTAL PROTOTYPE AND MEASUREMENT

In this article, a 200-W prototype, as shown in Fig. 17(a), was built, and the specifications and main components are listed in Table II. The parameters of the air-core inductors, including the inductive coupler, are already given in Table I. Notably, the distance between the transmitting coil and the receiving coil is 10 mm, with a coupling coefficient of $k = 0.24$ when the transmitting and receiving coils are aligned. Fig. 17(b) shows the measurement setup when the system is running.

A. Inductive Coupler Measurement Results

Fig. 18 presents the inductive coupler measurement results, including the mutual inductance and coupling factor by impedance analyzer Agilent 4294 A. It can be observed that when the receiver locates within the free-positioning region (lateral misalignment $\delta < 25$ mm), the mutual inductance and coupling coefficient of the inductive coupler can keep almost constant, which validates the design of homogeneous-flux transmitting coil.

B. Circuit Test Results

The circuit test results, which include the output power and efficiency of the system under various misalignments of the inductive coupler, are presented in Fig. 19. The input voltage and resistive load were held constant as $V_{\text{in}} = 48$ V and $R_l = 10.5\,\Omega$, respectively. It can be concluded that the proposed transmitting coil enables the built IPT system to exhibit high misalignment tolerance, wherein the output power and system efficiency remain nearly constant, provided that the receiver is situated within the free-positioning region (lateral misalignment $\delta < 25$ mm).

Figs. 20 and 21 present the operating waveforms of the system, revealing that the ZVS of the switching devices in the inverter is maintained despite misalignment. Moreover, the symmetry waveform of the drain-source voltage indicates that the power processed by each phase of the push–pull class-E inverter is balanced. Keeping input voltage as $V_{\text{in}} = 48$ V and gradually increasing the resistive load from 10 to 150 Ω, the efficiency of the system at different load conditions can be obtained, as shown in Fig. 22. The efficiency will exceed 85% when the transmission power is over 75 W, and a peak efficiency of 89.0% is achieved. In addition, it can be found that even though there is a 25-mm misalignment between the transmitting coil and receiving coil, the efficiency of the system is almost same as the case when the transmitting coil and receiving coil are aligned. Fig. 23 illustrates the losses breakdown of the converter operating at the rated power output ($P_r = 200$ W). 29% of losses are dissipated on the inductive coupler. Compared to the push–pull class-E inverter, the passive push–pull class-E rectifier dissipated 15% more losses. Using a synchronous active class-E rectifier could reduce the losses at the expense of increasing the cost and the system complexity, since the phase detect circuit and gate driver circuit are required for a synchronous rectifier.

C. Comparison With Existing WPT Systems for UAVs

Table III presents a comparison of the performance of wireless charging systems for UAVs, as reported in recent literature. Based on the data provided in the table, it can be found that the proposed IPT system exhibits competitive advantages owing to its superior efficiency and high misalignment tolerance.

VI. CONCLUSION

This article presents an optimization study of a 6.78 MHz IPT system for UAVs. The study utilizes a push–pull class-E inverter/rectifier and an LCC-S compensated coupled coil to achieve ZPA impedance and load-independent features. To improve the misalignment tolerance of the system, a homogeneous-flux transmitting coil is designed. The optimal allocation of the transmitting coil turns is obtained by combining the magnetic field model and an optimization algorithm. In addition, an analytical eddy-current loss model is proposed and verified by simulation. The errors for the spiral and helical coils are 7.1% and 4.9%, respectively. Using the analytical loss model, the parameters of all the air-core inductors used in this study are optimized. Finally, a 6.78 MHz 200-W IPT system with a homogeneous-flux transmitting coil is demonstrated. The inductive coupler measurement results show that the coupling coefficient and mutual inductance of the coupler remain almost constant when the receiver is located in the free-positioning region (lateral misalignment $\delta < 25$ mm). The circuit test results demonstrate that the system can maintain a 200-W output power and 89% efficiency with a 25-mm lateral misalignment. Based on the experimental results, it can be concluded that the

proposed IPT system achieves high-misalignment-tolerance and high-efficiency characteristics.

APPENDIX

With the built magnetic field model, the self-inductance of the coil can be calculated by

$$L_{\text{self}} = \frac{\Phi_{\text{self}}}{I} = \frac{\sum_{k=1}^{n} \iint_{S(k)} \vec{B} \mathrm{d}S}{I} \tag{A.1}$$

where, n denotes the number of turns of the coil, $S(k)$ represents the coverage region of each turn of the coil, I is the unit current flowing through the coil, $\vec{B}$ is the magnetic field generated by the coil itself.

REFERENCES

[1] E. Karakose, "Performance evaluation of electrical transmission line detection and tracking algorithms based on image processing using UAV," in *Proc. Int. Artif. Intell. Data Process. Symp.*, 2017, pp. 1–5, doi: 10.1109/IDAP2017.8090302.

[2] J. Zhou, B. Zhang, W. Xiao, D. Qiu, and Y. Chen, "Nonlinear parity-time-symmetric model for constant efficiency wireless power transfer: Application to a drone-in-flight wireless charging platform," *IEEE Trans. Ind. Electron.*, vol. 66, no. 5, pp. 4097–4107, May 2019, doi: 10.1109/TIE.2018.2864515.

[3] T. He, Y. Zeng, and Z. Hu, "Research of multi-rotor UAVs detailed autonomous inspection technology of transmission lines based on route planning," *IEEE Access*, vol. 7, pp. 114955–114965, 2019, doi: 10.1109/ACCESS.2019.2935551.

[4] C. Cai, S. Wu, L. Jiang, Z. Zhang, and S. Yang, "A 500-W wireless charging system with lightweight pick-up for unmanned aerial vehicles," *IEEE Trans. Power Electron.*, vol. 35, no. 8, pp. 7721–7724, Aug. 2020, doi: 10.1109/TPEL.2020.2964023.

[5] T. Alladi, G. Naren, V. B. Chamola, and M. Guizani, "SecAuthUAV: A novel authentication scheme for UAV-ground station and UAV-UAV communication," *IEEE Trans. Veh. Technol.*, vol. 69, no. 12, pp. 15068–15077, Dec. 2020, doi: 10.1109/TVT.2020.3033060.

[6] S. Wu, C. Cai, L. Jiang, J. Li, and S. Yang, "Unmanned aerial vehicle wireless charging system with orthogonal magnetic structure and position correction aid device," *IEEE Trans. Power Electron.*, vol. 36, no. 7, pp. 7564–7575, Jul. 2021, doi: 10.1109/TPEL.2020.3047384.

[7] M. Atif, R. Ahmad, W. Ahmad, L. Zhao, and J. J. P. C. Rodrigues, "UAV-assisted wireless localization for search and rescue," *IEEE Syst. J.*, vol. 15, no. 3, pp. 3261–3272, Sep. 2021, doi: 10.1109/JSYST.2020.3041573.

[8] G. Aiello, F. Hopps, D. Santisi, and M. Venticinque, "The employment of unmanned aerial vehicles for analyzing and mitigating disaster risks in industrial sites," *IEEE Trans. Eng. Manag.*, vol. 67, no. 3, pp. 519–530, Aug. 2020, doi: 10.1109/TEM.2019.2949479.

[9] A. M. Jawad, H. M. Jawad, R. Nordin, S. K. Gharghan, N. F. Abdullah, and M. J. Abu-Alshaeer, "Wireless power transfer with magnetic resonator coupling and sleep/active strategy for a drone charging station in smart agriculture," *IEEE Access*, vol. 7, pp. 139839–139851, 2019, doi: 10.1109/ACCESS.2019.2943120.

[10] P. K. Chittoor, B. Chokkalingam, and L. Mihet-Popa, "A review on UAV wireless charging: Fundamentals, applications, charging techniques and standards," *IEEE Access*, vol. 9, pp. 69235–69266, 2021, doi: 10.1109/ACCESS.2021.3077041.

[11] A. Ahmad, M. S. Alam, and R. Chabaan, "A comprehensive review of wireless charging technologies for electric vehicles," *IEEE Trans. Transport. Electrific.*, vol. 4, no. 1, pp. 38–63, Mar. 2018, doi: 10.1109/TTE.2017.2771619.

[12] S. Aldhaher, P. D. Mitcheson, J. M. Arteaga, G. Kkelis, and D. C. Yates, "Light-weight wireless power transfer for mid-air charging of drones," in *Proc. IEEE 11th Eur. Conf. Antennas Propag.*, 2017, pp. 336–340, doi: 10.23919/EuCAP.2017.7928799.

[13] J. M. Arteaga, S. Aldhaher, G. Kkelis, C. Kwan, D. C. Yates, and P. D. Mitcheson, "Dynamic capabilities of multi-MHz inductive power transfer systems demonstrated with batteryless drones," *IEEE Trans. Power Electron.*, vol. 34, no. 6, pp. 5093–5104, Jun. 2019, doi: 10.1109/TPEL.2018.2871188.

[14] H. Zhang, Y. Chen, C.-H. Jo, S.-J. Park, and D.-H. Kim, "DC-link and switched capacitor control for varying coupling conditions in inductive power transfer system for unmanned aerial vehicles," *IEEE Trans. Power Electron.*, vol. 36, no. 5, pp. 5108–5120, May 2021, doi: 10.1109/TPEL.2020.3032155.

[15] Z. Bie, J. Zhang, K. Song, D. Wang, and C. Zhu, "A free-rotation asymmetric magnetic coupling structure of UAV wireless charging platform with conformal pickup," *IEEE Trans. Ind. Electron.*, vol. 69, no. 10, pp. 10154–10161, Oct. 2022, doi: 10.1109/TIE.2022.3165297.

[16] Y. Li et al., "A new magnetic coupler with high rotational misalignment tolerance for unmanned aerial vehicles wireless charging," *IEEE Trans. Power Electron.*, vol. 37, no. 11, pp. 12986–12991, Nov. 2022, doi: 10.1109/TPEL.2022.3184335.

[17] P. Cao et al., "Embedded lightweight squirrel-cage receiver coil for drone misalignment-tolerant wireless charging," *IEEE Trans. Power Electron.*, vol. 38, no. 3, pp. 2884–2888, Mar. 2023, doi: 10.1109/TPEL.2022.3225307.

[18] J. Wang, R. Chen, C. Cai, J. Zhang, and C. Wang, "An onboard magnetic integration-based WPT system for UAV misalignment-tolerant charging with constant current output," *IEEE Trans. Transport. Electrific.*, vol. 9, no. 1, pp. 1973–1984, Mar. 2023, doi: 10.1109/TTE.2022.3200039.

[19] Y. Shao, N. Kang, H. Zhang, R. Ma, M. Liu, and C. Ma, "A lightweight and robust drone MHZ WPT system via novel coil design and impedance matching," *IEEE Trans. Ind. Appl.*, vol. 59, no. 3, pp. 3851–3864, May/Jun. 2023, doi: 10.1109/TIA.2023.3249146.

[20] T. M. Mostafa, A. Muharam, and R. Hattori, "Wireless battery charging system for drones via capacitive power transfer," in *Proc. IEEE PELS Workshop Emerg. Technol.: Wireless Power Transfer*, 2017, pp. 1–6, doi: 10.1109/WoW.2017.7959357.

[21] D. Vincent, P. S. Huynh, L. Patnaik, and S. S. Williamson, "Prospects of capacitive wireless power transfer (C-WPT) for unmanned aerial vehicles," in *Proc. IEEE PELS Workshop Emerg. Technol.: Wireless Power Transfer*, 2018, pp. 1–5, doi: 10.1109/WoW.2018.8450918.

[22] H. Zhang, C. Zhu, S. Zheng, Y. Mei, and F. Lu, "High power capacitive power transfer for electric aircraft charging application," in *Proc. IEEE Nat. Aerosp. Electron. Conf.*, 2019, pp. 36–40, doi: 10.1109/NAECON46414.2019.9057957.

[23] M. Lu, M. Bagheri, A. P. James, and T. Phung, "Wireless charging techniques for UAVs: A review, reconceptualization, and extension," *IEEE Access*, vol. 6, pp. 29865–29884, 2018, doi: 10.1109/ACCESS.2018.2841376.

[24] J. M. Arteaga, S. Aldhaher, G. Kkelis, D. C. Yates, and P. D. Mitcheson, "Multi-MHz IPT systems for variable coupling," *IEEE Trans. Power Electron.*, vol. 33, no. 9, pp. 7744–7758, Sep. 2018, doi: 10.1109/TPEL.2017.2768244.

[25] M. Liu, H. Zhang, Y. Shao, J. Song, and C. Ma, "High-performance megahertz wireless power transfer: Topologies, modeling, and design," *IEEE Ind. Electron. Mag.*, vol. 15, no. 1, pp. 28–42, Mar. 2021, doi: 10.1109/MIE.2020.3002516.

[26] S.-C. Wong and C. Tse, "Design of symmetrical class E power amplifiers for very low harmonic-content applications," *IEEE Trans. Circuits Syst. I: Reg. Papers*, vol. 52, no. 8, pp. 1684–1690, Aug. 2005, doi: 10.1109/TCSI.2005.851723.

[27] X. Huang, Z. Yu, Y. Dou, S. Lin, Z. Ouyang, and M. A. E. Andersen, "Load-independent push-pull class E^2 topology with coupled inductors for MHz-WPT applications," *IEEE Trans. Power Electron.*, vol. 37, no. 7, pp. 8726–8737, Jul. 2022, doi: 10.1109/TPEL.2022.3150175.

[28] S. Aldhaher, D. C. Yates, and P. D. Mitcheson, "Load-independent class E/EF inverters and rectifiers for MHz-switching applications," *IEEE Trans. Power Electron.*, vol. 33, no. 10, pp. 8270–8287, Oct. 2018, doi: 10.1109/TPEL.2018.2813760.

[29] X. Huang, Y. Dou, S. Lin, Y. Tian, Z. Ouyang, and M. A. E. Andersen, "Synchronous push-pull class E rectifiers with load-independent operation for megahertz wireless power transfer," *IEEE Trans. Power Electron.*, vol. 36, no. 6, pp. 6351–6363, Jun. 2021, doi: 10.1109/TPEL.2020.3038814.

[30] J. Ferreira, "Improved analytical modeling of conductive losses in magnetic components," *IEEE Trans. Power Electron.*, vol. 9, no. 1, pp. 127–131, Jan. 1994, doi: 10.1109/63.285503.

[31] J. Mühlethaler, "Modeling and multi-objective optimization of inductive power components," Ph.D. dissertation, ETH Zurich, Zuürich, Switzerland, 2012.

Jiasheng Huang (Graduate Student Member, IEEE) received the B.S. degree from Fuzhou University, Fuzhou, China, in 2017, and the M.Sc. degree from Xi'an Jiaotong University, Xi'an, China, in 2020, both in electrical engineering. He is currently working toward the Ph.D. degree in power electronics with the Technical University of Denmark, Kongens Lyngby, Denmark.

His research interests include design of high-frequency resonant converters and modeling and optimization of MHz-range wireless power transfer systems.

Yi Dou (Member, IEEE) received the M.Sc. and Ph.D. degrees in power electronics from the Technical University of Denmark, Kongens Lyngby, Denmark, in 2018 and 2022, respectively.

He is a Senior Power Electronics Engineer with Resonant Link Inc., South Burlington, VT, USA. He is focusing on research and development in wireless power transfer systems for implanted medical devices. His research interests include design of high frequency dc–dc converters, modeling, and design for magnetic components, and modeling and optimization of MHz-range wireless power transfer systems.

Xiaosheng Huang (Member, IEEE) received the B.E. and Ph.D. degrees in electrical engineering from Fuzhou University, Fuzhou, China, in 2009 and 2015, respectively.

He is currently an Associate Professor with the School of Electronic, Electrical Engineering and Physics, Fujian University of Technology, Fuzhou, China. His research interests include power conversion, high-frequency magnetics, wireless power transfer, and electromagnetic field analysis and applications.

Dr. Huang is a Member of the Magnetic Component Specialty Committee of the China Power Supply Society.

Zhe Zhang (Senior Member, IEEE) received the B.Sc. and M.Sc. degrees in power electronics from Yanshan University, Qinhuangdao, China, in 2002 and 2005, respectively, and the Ph.D. degree in power electronics from the Technical University of Denmark (DTU), Kongens Lyngby, Denmark, in 2010.

From 2014–2021, he was an Associate Professor with the Department of Electrical Engineering, DTU. He has authored or coauthored more than 200 publications. His research interests include applications of wide bandgap devices, high-frequency dc–dc converters, dc–ac inverters, high-frequency magnetics for renewable energy systems, hybrid electric vehicles, high-temperature power solutions, and wireless power transferring.

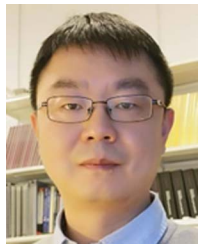

Ziwei Ouyang (Senior Member, IEEE) received the Ph.D. degree from the Technical University of Denmark (DTU), Kongens Lyngby, Denmark, in 2011.

Since April 2016, he has been an Associate Professor with DTU. He has authored or coauthored more than 100 high impact IEEE journal and conference publications, and nine international patents. His research interests include switch mode power supply, magnetics modeling and integration, energy storage system, and wireless charging.

Dr. Ouyang was a recipient of the 2021 IEEE Transactions on Power Electronics First Place Prize Paper Award, and several Best Paper Awards in IEEE sponsored international conferences.

Michael A.E. Andersen (Member, IEEE) received the M.Sc.E.E. and Ph.D. degrees in power electronics from the Technical University of Denmark, Kongens Lyngby, Denmark, in 1987 and 1990, respectively.

He is currently a Professor of power electronics with the Technical University of Denmark, where he has been Deputy Head of Department of Electrical Engineering, from 2009 to 2022. He has authored or coauthored more than 300 publications. His research interests include switch-mode power supplies, piezoelectric transformers, power factor correction, switch-mode audio power amplifiers, and VHF power converters.